Reaction Chemistry & Engineering

Experimental and Computational Study of Particle Formation Kinetics in UF6 Hydrolysis

Journal:	*Reaction Chemistry & Engineering*
Manuscript ID	RE-ART-05-2020-000207.R1
Article Type:	Paper
Date Submitted by the Author:	04-Jul-2020
Complete List of Authors:	Cheng, Meng-Dawn; Oak Ridge National Laboratory, Richards, Jason; Oak Ridge National Laboratory Omana, Michael; Sandia National Laboratories Hubbard, Joshua; Sandia National Laboratories Fugate, Glenn; Oak Ridge National Laboratory

ARTICLE

Received 00th January 20xx,

Accepted 00th January 20xx

DOI: 10.1039/x0xx00000x

Experimental and Computational Study of Particle Formation Kinetics in UF_6 Hydrolysis

Meng-Dawn Cheng,*[a] Jason M. Richards [b], Michael A. Omana[c], Joshua A. Hubbard[d], and Glenn A. Fugate [b]

The formation and growth of UO_2F_2 particles by gas-phase UF_6 hydrolysis remains of interest to actinide chemistry research. The total number concentration of the UO_2F_2 aerosol particles that can be produced in the reaction is regulated primarily by the availability of water molecules in our reactor conditions. Increase in water molecule concentration corresponds with a higher amount and larger size of UO_2F_2 aerosol particles produced. The growth rates of aerosol particles appear to approach a single number in the range of [0.05 ± 0.03 - 0.08 ± 0.04] (nm/s), as the molar ratio of water to UF_6 decreases below 1. The size of primary particles produced from the UF_6 hydrolysis in the water-deprived condition was estimated to be 3.6 ± 0.4 nm. At the molar ratio becomes greater than 1.7, the size of primary particles increased with increased availability of water molecule. The primary particle model developed in this work predicted a size range for the UO_2F_2 primary particles similar to that estimated based on the data from the gas-phase UF_6 hydrolysis experiments. This result suggests that the volume-driven coalescence process assumption used in the derivation of the primary particle model was reasonable. The ability to precisely control the availability of water molecules and reaction time could lead to the production of nearly monodispersed aerosol particles. This finding has significant implications in the engineering manufacturing of fuel powder materials and possibly to future development and deployment of environmental sampling apparatus.

1. Introduction

The uranyl ion forms solid salt species (e.g., UO_2F_2) (called particles or particulate matter hereafter) that are generally not a commodity to nuclear industry but it plays a key intermediate role in uranium hexafluoride (UF_6) applications; e.g., in the production of uranium dioxide (UO_2) powder for nuclear fuel production[1,2] or in the verification of weapons declarations as a unique tracer for nuclear sites.[3,4] Therefore, it is of great importance to improve our understanding of the formation mechanism and the evolution of properties of this particulate species in nuclear manufacturing processes and its fate as they are produced in relevant environmental conditions.

It has been known for several decades that UO_2F_2 particles are produced when UF_6 is in contact with water vapor (H_2O).[5,6,7,8,9,10,11,12] UF_6 hydrolysis produces solid UO_2F_2 particles and also hydrogen fluoride (HF), a hazardous toxic gas, as written in the following equation:

$$UF_6(g) + 2\ H_2O(g) \rightarrow UO_2F_2(s) + 4\ HF(g) \quad (1)$$

[a] Environmental Sciences Division, Oak Ridge National Laboratory, Oak Ridge, Tennessee, USA.
[b] Isotope and Fuel Cycle Technology Division, Oak Ridge National Laboratory, Oak Ridge, Tennessee, USA.
[c] Monitoring Systems Center, Sandia National Laboratories, Albuquerque, New Mexico, USA.
[d] Engineering Sciences Center, Sandia National Laboratories, Albuquerque, New Mexico, USA.

Eq. (1) generally serves as the basis in predicting the reaction-generated HF concentration for consequence analysis in environmental management and safety of UF_6 storage and operation, particularly in industry where environmental safety and health concerns were caused by the hazardous gas HF.[13,14,15,16,17,18] The intermediate by-product UO_2F_2 is typically of less interest but has been suggested for use as a tracer for identifying sources involving in nuclear fuel processing and nuclear forensics.[3,4]

Recently, Hu et al.[19,20,21] used the relativistic density function theory to show, computationally, that intermediate species containing U-O-U bond were found because of several probable reactions involving UF_5OH and UF_6 or UF_5OH and UF_5OH under the condition of enriched UF_6 and small amounts of H_2O (i.e., small ω condition) where ω is the molar ratio of H_2O to UF_6. In large ω conditions, the coordination energy between UF_6 and $(H_2O)_n$ in UF_6-nH_2O (e.g., where n = 1–3) increases as water changes from single molecules to the associated dimer and trimer. These computational studies suggest that the initial step of UF_6 hydrolysis led first to one H_2O molecule to coordinate with uranium as a ligand of UF_6. Additional one or two H_2O molecules then enhanced the coordination through hydrogen bonding with ligand H_2O and F. Second, the additional H_2O molecules catalyzed UF_6 hydrolysis by bridging the hydrogen that transfers from ligand H_2O to F and stabilizes the transition state through hydrogen bonding. The additional H_2O molecules associate the products of the hydrolysis, UF_5OH and HF, through hydrogen bonding. The eliminated HF was then removed depending on the water content and bonding types of the reaction products.

When $\omega \geq 3$, the first step of hydrolysis becomes exothermic, but the HF tends to associate with UF_5OH and H_2O tightly. Lind et al.[2] showed that hydrolysis of one UF_6 and 2 H_2O molecules is the favorable pathway as a tri-molecular reaction. One water molecule provides the hydrogen to the nascent HF in the transition state that accepts one hydrogen from the other water molecule that is reacting with UF_6 to form UF_5OH. No mechanistic information, computationally or experimentally, was given that could lead to a concrete conclusion about the production of UO_2F_2.

None of these molecular modelling works[19,20,21,2] directly suggest the pathway of UO_2F_2 aerosol formation. The aerosol formation process and kinetics remain unknown. We have systematically investigated the formation kinetics of UO_2F_2 particles and derived the size of primary particle diameter, the formation rate, and the subsequent growth of the produced particles in an aerosol reactor. This paper describes the aerosol reaction engineering portion of the study.

2. Materials and methods

2.1. Aerosol reactor

The aerosol reactor was designed and constructed in house for the study. Figure 1 illustrates the columnar aerosol reactor used to perform controlled UF_6 hydrolysis experiments in the gas-phase. The reactants, UF_6 and H_2O, were introduced in a carrier gas at 1 Litre per minute (LPM) flow rate each through a 0.32 cm ID tube at the opposing direction at the upper section of the reactor. The separation distance of the two tube tips was approximately 4 cm. This arrangement promotes the mixing of the reactants. The exhaust from the reactor is at the bottom in the lower section of the reactor and was vacuum pumped directly to a mitigation system shown in Figure 2. The mitigation system consisted of an alumina packed tube and a High Efficiency Particulate Air (HEPA) filter. The pressure inside the reactor was continuously monitored with a Dwyer Magnehelic gauge and maintained at zero cm-H_2O or a slightly negative pressure.

The reactor was a cylinder fabricated from stainless steel and was 103 cm in length and 15.24 cm in inner diameter. The reactor consisted of two body sections that were Viton O-ring sealed in the middle with six flanges to clamp both sections together. The two sections can be separated to allow reactor maintenance and future modification if desired. A 2.54 cm thick honeycomb mesh with 0.079 cm size cells was inserted at the top of the reactor above a diffuser plate to generate laminar flow of carrier gas

that was introduced from the top. The diffuser plate was used to block about 25% of the cross-sectional area in the center of the reactor directly behind the honeycomb. This created a lower pressure cavity region for facilitating reactant mixing. There were 3 pairs of optical CaF_2 window ports for optical and spectroscopic observations, while 3 pairs of extractive sampling ports (labelled as U, M, and L in Figure 1) were positioned along the column length of the aerosol reactor.

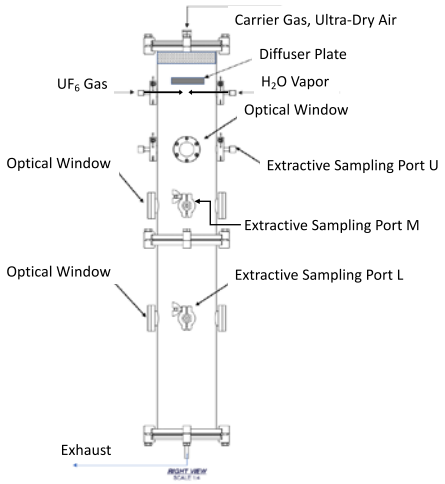

Figure 1. Schematic Drawing of Aerosol Reactor

The hydrolysis reaction occurs when UF_6 and H_2O are mixed. The residual reactants and reaction products, UO_2F_2 and HF, were transported by the carrier gas, an ultra-dry air, down the reactor column toward the exhaust. The ultra-dry air was generated by a Parker ultra-dry air generator (Model UDA-300). The flow rate of the ultra-dry carrier gas varied between 20 and 50 LPM dependent on an experiment.

Figure 2 is the schematic drawing of the entire experimental setup and the aerosol reactor, consisting of four components, the UF_6 release module, the aerosol reactor, the water vapor source, and finally the exhaust mitigation module. Not included in the setup drawing is the array of instruments installed on the reactor for observations. In this paper we will present data from a commercial instrument called the Scanning Mobility Particle Sizer (SMPS)[22,23] available from TSI, Inc. The UF_6 release and mitigation modules are the only two that are required by the United States Department of Energy Environmental Safety and Health (ESH) regulations to be in a fume hood based on the material quantity used in this study. The aerosol reactor was operated as a non-rad component outside of the hood. The alumina column was used to remove HF and residual UF_6, while a HEPA filter capsule was used to remove residual particles before the exhaust going into the hood and ventilated. The exhaust of each instrument (e.g., SMPS) that extracted sample from the aerosol reactor was routed through a mitigation module that was comprised of a HEPA filter and an alumina-packed tube before the exhaust was vented back to the hood. This mitigation module is for instrument exhaust only, separate from the treatment module for the reactor described earlier. The diligent mitigation precaution was taken to reduce the potential ESH risks faced when working with radiological and hazardous materials.

A manifold was designed to allow delivery of controlled flows of UF_6 over a wide range of concentrations. The system can be purged with inert air and evacuated to allow for the system to be thoroughly dried to remove all water. The gas stream was split using two mass flow controller units (MKS), allowing the UF_6 gas stream to be diluted up to several orders of magnitude as needed. The initial UF_6 stream was generated from sublimation of solid in the first U-tube which was held at ambient temperatures. The solid-gas equilibrium at 25°C generated a partial pressure approaching saturation of ~112 Torr[24]. This UF_6 laden gas stream then passed through the second U-tube that was chilled to condense material. This effectively reduced the gas concentration to a steady, adjustable concentration that was dependent on the temperature of the U-tube. This UF_6 gas composition was monitored with a Bruker Fourier-Transformed InfraRed (FTIR) spectrometer (Bruker Model ALPHA) using one or more of the spectral bands. The measurement was performed before dilution of the gas to its final desired composition as some of the target concentrations may be below the detection ability of the FTIR spectrometer. The UF_6 concentration was maintained at 100 ppm for all the data presented in this paper.

Water vapor was generated by using the trace source permeation technique using an instrument

manufactured by Kin-Tek (Model: Span Pac™ H_2O). The technique is capable of generating moisture trace standards from 100 ppb to 100 ppm. The Span Pac™ H_2O generator holds the trace sources permeation tube at a constant temperature and introduces a controlled flow of dilution gas over the tube.

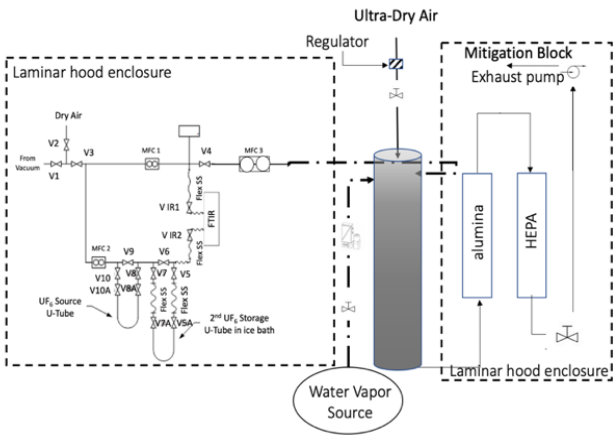

Figure 2. Schematic Drawing of Experimental Setup

A small, accurate, constant flow of H_2O vapor permeated from the tube was mixed with the dry dilution gas to form the ppm or ppb moisture standard. The moisture standard then flowed through the generator output to a monitor probe. The flow of the water vapor to the reactor was set at 1 LPM, same as that of the UF_6 flow rate into the aerosol reactor.

For higher concentrations of water, the relative humidity (RH) was maintained using a split flow system. A valve was used to divert a fraction of the flow through a sparger submerged in distilled water. The wetted gas was recombined with the dry gas, passed through a droplet collection vessel, and then flowed past a relative humidity probe. The valve was adjusted to select the desired RH. The RH was monitored online by a Vaisala hygrometer (Model MI70). The concentration of the water vapor was then adjusted for temperature to provide a true concentration being fed to the system.

3. Results and discussion

3.1. Particle size distributions

The observed size distributions of the UO_2F_2 particles were produced in experiments controlled by changing the **ω** values. Note that **ω**= molar ratio of $[H_2O]/[UF_6]$. The brackets [H2O] and [UF6] indicate the concentrations in mol*L^{-1} of water and uranium hexafluoride, respectively. The distributions observed by the SMPS are displayed in Figures 3 and 4. The SMPS consists of a TSI Model 3082 electrical classifier, equipped with a nano-Differential Mobility Analyzer (nano-DMA, TSI Model 3085A), a soft X-ray charge neutralizer (TSI model 3088), and a 3788 Nanowater-based condensation particle counter. The instrument sheath flow rate was set at 15 LPM while the aerosol sampling flow rate was 1.5 LPM throughout all experiments. Each curve is an average of 27 - 28 measurements for a given condition. The coefficient of variation (mean over standard deviation) for each curve varies between ± 1-20% dependent on the particle size. The total scanning time for each curve was 60 seconds that included the up- and down-scan times.

Figure 3 shows the particle size distributions observed for **ω** values of 370 and 6250, water-rich conditions, which are approximately 5% and 84% RH, respectively, at 1 atm and room temperature. Figure 4 shows **ω** values of 1 and 0.005, which corresponds to 100 ppm and 0.5 ppm H_2O concentration, respectively. Figure 4 contrasts results obtained from water-deprived conditions to those in the water-rich ones in Figure 3.

As displayed in Figure 3, the UO_2F_2 particles exhibit broad size distributions with the aerosol mobility diameter spanning from 2.5 to 90 nm. The high the humidity, the larger the size of the particles. For example, a water vapor concentration of 774.410 ppm at 298 K and 1013.5 mbar (or 5% RH at the given temperature and pressure) has a ω of value of 370, for example. As shown in Figure 3, the peak size for ω= 6250 was approximately 12 nm at the sampling port U, while that for ω = 8 nm observed at the same port for ω= 370.

As the produced particles traversed down the reactor column, we believe reaction might be continuously occurring between the residual trace UF_6 and abundant water molecules. The subsequent reactions possibly involved HF monomers that were produced from the hydrolysis reaction and HF oligomers from the polymerization of the HF monomers causing fog formation.[25] These reactions

involving HF monomers and oligomers could occur on the surfaces of formed UO_2F_2 aerosol particles complicating the chemical composition and shape of aerosol particles, according to Hou et al.[1]

As shown in Figure 3, the peak size of a population curve increased from the port U to L as reflected in the right-shift of the peak size of each distribution. The growth in the distribution from 12 nm at the sampling port U to 20 nm at port L for ω=6250 vs. 8 nm at port U to 12 nm at the port L for ω=370 was remarkable. We will discuss the growth rate in a later Section 3.2.

One additional observation was the decrease in the peak height of the corresponding curve at the sampling port location L comparing to that observed at the location U or M. The relative reduction in peak height from U to L for ω=370 was about 34%, while that for ω=6250 was 18%. Also, the availability of water in the condition of ω=6250 was higher than that in ω of 370, which could lead to more reduction in the number of UO_2F_2 particles observed at all three ports due to condensation and coalescence processes, which are particle number reduction processes. Note that these high ω conditions are environmentally relevant, but this is the first time that aerosol particle size distributions have been systematically measured, and the aerosol dynamics observed, experimentally.

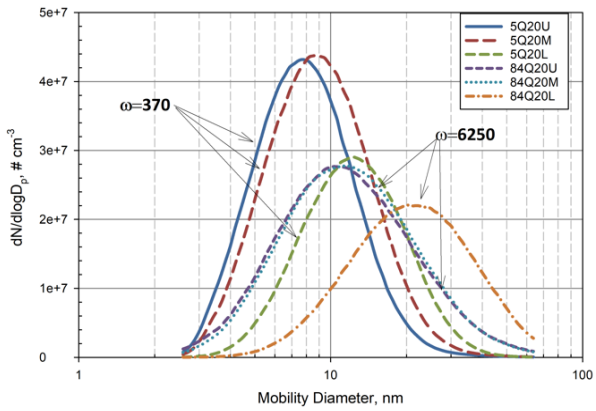

Figure 3. Particle Mobility Size Distributions for Larger **ω** Values. The legend U, M, and L shows the sampling location where U is the upper sampling port most close to the point where UF_6 and H_2O were mixed, M is the middle port, and L is the port that is farther away from the mixing point.

Figure 4 displays the SMPS curves obtained for the experimental conditions where the water molecule concentrations were limited in relation to UF_6; i.e., in the region where the **ω** values were less than or equal to 1. For example, in the case of **ω** = 0.005, water availability to UF_6 molecules was severely limited because the absolute concentration of water molecules in the condition was 503 ppb in relation to 100,000 ppb of UF_6 gas molecules. Also note that these water-deprived conditions are generally rare in the environment but were studied as part of our systematic investigation.

A couple of observations are made about the water-deprived SMPS curves. One is that the range of particle diameter in Figure 4 was several times smaller than that reported in Figure 3. The peak sizes of the SMPS curves in Figure 4 were all less than 10 nm. This is a stark contrast to the curves displayed in Figure 3 where the peak diameter of the particle population grew to sizes larger than 10 nm.

Also, the peak heights in Figure 4 are much smaller than those observed in the larger- **ω** conditions clearly indicating the adverse impacts of water availability on the aerosol formation, because the available UF_6 concentration in these experiments were identical.

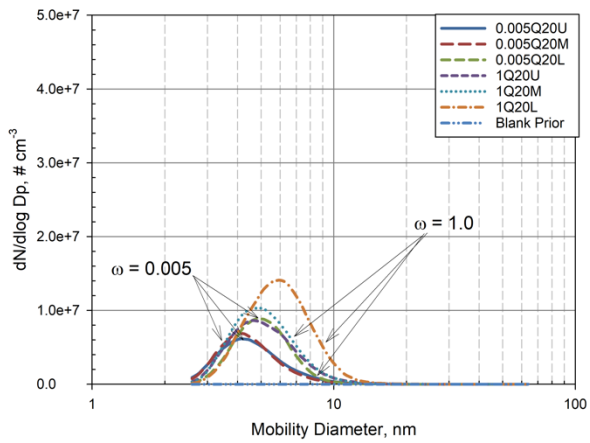

Figure 4. Particle Mobility Size Distribution for Smaller **ω** Values. Legend "Blank Prior" indicates the blank concentration or background aerosol concentration in the reactor prior to the start of an experiment. Note the highest value on the Y-axis is approximately 3X smaller than that in Figure 3a.

There were other interesting observations in Figure 4 in comparison to Figure 3. The peak diameters of all the aerosol populations represented

in Figures 3 and 4 shifted toward the larger size as observations were moved from the sampling port U to L. This size growth is indictive of a rapid aging effect of the produced aerosol population as it travels down the reactor column from the port U to L. The growth of the peak diameter for the two small **ω** conditions was not as significant as that found in the large **ω** conditions. This could be because the amount of water molecules available to coalesce and grow the formed particles was limited in the water-deprived conditions. In fact, the peak diameter growth was merely 1 nm ranging from 4 at the port U to 5 nm at the port L for **ω**=0.005 and also about 1 nm from 5 nm at the port U to 6 nm at port L for **ω**=1. Again, this level of growth of UO_2F_2 particles in the aerosol reactor is negligible and could be directly attributed to the result of water molecule shortage in relation to UF_6 in the small-**ω** conditions.

Now, the population growth pattern from the sampling port U to L in Figure 4 is different from that observed in Figure 3. In the water-deprived region, the number of particles appears to increase as the flow traversed from the port U to L, as opposed to the decreasing trend shown in Figure 3. We interpreted the decreasing trend in Figure 3 as a result of coalescence and coagulation processes.

However, in the very dry conditions, few water molecules were available for the condensational growth. Since the reaction time constant (in nanoseconds) is much smaller than that of the coalescence (in milliseconds), the number of particles formed by the reaction would conceivably increase at a higher rate than that was reduced by the coalescence in the small **ω** conditions. Thus, we observed a reversed trend in the growth of total number concentrations in two very different regimes of **ω**.

Again, more particles produced in the "dry" conditions led to the increase of total number concentration; the number increase would also promote coagulation/aggregation processes. The number increase, though small, could contribute to the 1-nm increase in the peak diameter of the population that was detected. It is important to mention, though, the chemical composition of the aerosol particles might be significantly distinct in the two dramatically different **ω** regimes. This remains a topic in our future study.

Summarizing the results shown in Figures 3 and 4, we conclude that the formation and growth of aerosol particle size by UF_6 hydrolysis in the gas-phase is strongly dependent on the availability of water molecules. Furthermore, the total number concentration (i.e., the area under a curve) of the UO_2F_2 particulate material produced is also regulated by the availability of water vapor concentration. The higher the water vapor concentration, the higher number and larger in size of the UO_2F_2 aerosol particles. Controlling the availability of water molecule in the UF_6 hydrolysis reaction could lead to the production of a nearly monodispersed aerosol particles. In other words, the coherent result suggests that one can precisely manipulate the size of UO_2F_2 aerosol particles by controlling the water vapor availability and interaction of water molecules with UF_6 in the reaction. This finding has significant implication in the engineering manufacturing of fuel powder materials as well as environmental sampling apparatuses.

3.2. Particle growth and growth rate

As previously discussed in Section 3.1, aerosol dynamics were clearly observed in the reactor at the three sampling ports (U, M, and L). Since the average flow transient times (also called the elapsed time, τ) from the reaction center to these three ports were known [= (flow rate/cross-sectional area of the reactor)/distance between any two points along the reactor length], we could accurately calculate the UO_2F_2 particle growth rate based on the peak size of a SMPS curve observed (also called the Geometric Mean Diameter or GMD) at these ports in terms of τ between these ports. The GMD as a function of τ for various **ω** values are plotted in Figure 5.

As shown in Figure 5, the growth of aerosol particles in the reactor appears to follow a linear relationship with the reactor elapsed time (τ) for all **ω**. It is noted that the linear relationship holds from the time zero up to the first 30 seconds available in the aerosol reactor as shown in the X-axis. The linear relationship appears to converge or overlapping toward the small **ω** values. This supports once again

the particle growth is water-limited, a finding concluded in Section 3.1.

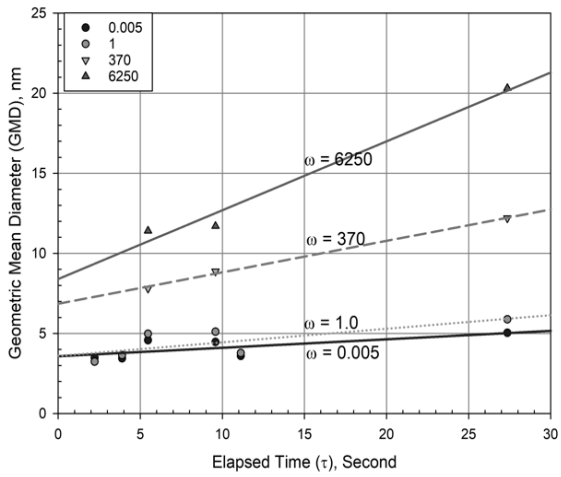

Figure 5. Particle Size Growth as a Function of Reactor Elapsed Time (τ) and Molar Ratio (ω) of a given reaction condition. The geometric mean diameter (GMD) of a SMPS curve is defined as the peak size of the particle size distribution curve.

The numeric values of derived linear regression results shown in Table 1 provide a clearer quantitative conclusion than that displayed in Figure 5. The relationship between the GMD and τ for a given **ω** is statistically robust as measured by the figure of merit R^2 value. Furthermore, the slope of each linear regression line represents the particle size growth rate (in the units of nm/s) and the intercept represents the initial size of particles or size of primary particles (in the units of nm).

Table 1. Linear Regression Results of the Curves Shown in Figure 4.

Molar Ratio, ω	Intercept (nm)	Slope (nm/s)	R^2
0.005	3.58 ± 0.34	0.05 ± 0.03	0.71
1.0	3.60 ± 0.48	0.08 ± 0.04	0.76
370	6.85 ± 0.20	0.20 ± 0.01	0.99
6250	8.40 ± 1.10	0.43 ± 0.07	0.99

Note: R^2 shows the figure of merit of the linear regression model. The R^2 values in Table 1 indicate the linear model fits data reasonably well.

The slope of the regression line increases as the **ω** value increased as shown in Table 1. In other words, the particle growth rate is increased when more water molecules are available to accelerate the aerosol dynamics. More interestingly, the growth rates (slopes) appear to approach a single number in the range of [0.05 ± 0.03 - 0.08 ± 0.04] (nm/s), statistically, as the molar ratio becomes small (e.g., **ω** = 1 and 0.005). Thus, it is likely there is a condition where the particle growth would flatten in the reactor irrespective of the molar ratio. We thus performed an interpolation calculation of the logarithmic data of the molar ratio and found that this condition is likely to be at **ω** of about 100 below which the particle growth rate is strongly restricted to approximately 0.1 nm/s.

3.3. Primary particles

Previous microscopic studies of UO_2F_2 formation produced many micrographs.[6,8,9,10,11,26] As the UO_2F_2 particles were produced, they were likely to be in a spherical shape at the beginning. Also, as a population these primary particles are likely to be monodispersed at the time of production. Depending on the reaction condition, availability of water molecules, the number of primary particles produced, as well as other factors (e.g., presence of foreign nuclei and or organic gas species), these primary particles would interact with each other and the additional factors leading eventually to a branched structure like the example shown in Figure 6. Figure 6 is adapted from Bostick et al.[6] from the UF_6 hydrolysis reaction at 2% RH condition. We do not know what the condition was in relation to the **ω** index value defined in Bostick et al. paper for comparison.

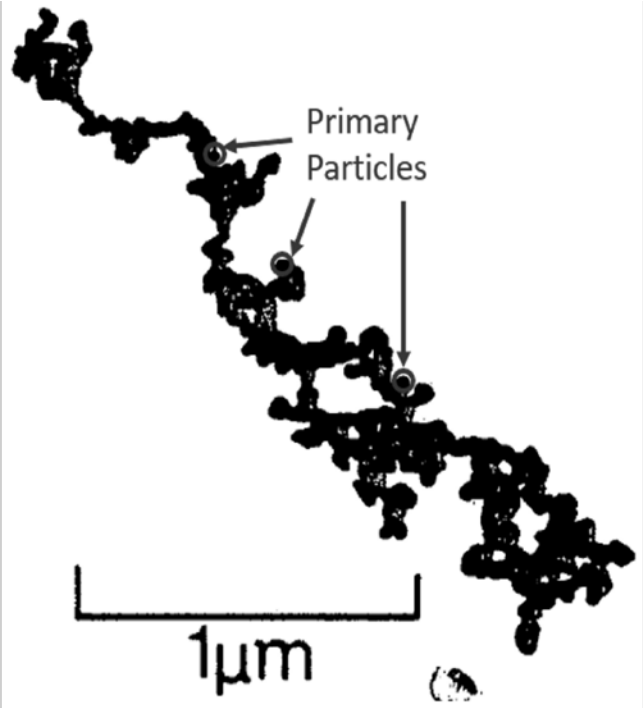

Figure 6. UO_2F_2 particle produced at less than 2% humidity (adapted from Bostic et al., 1984)

We used the data reported in the previous Sections to estimate the size of primary UO_2F_2 particles by using the linear regression-fit curves shown in Figure 5. If we assigned the elapsed time τ of 1 ns that is 10^{-9} sec after the hydrolysis reaction started, the data in the Intercept column in Table 1 show the plausible size of the primary particles produced by the hydrolysis reaction. The assumption made here was that the primary particles would form in 1 ns after the reaction started. This is a weak assumption in our numerical exercise, because increasing the τ value by 1,000,000 folds to 1 ms would not change the numerical values of the intercepts shown in Table 1 in any significant extent.

The linear regression model results show that the plausible size of primary particles appear to be dependent on the molar ratio **ω**; the higher the molar ratio, the larger the size of primary particles when the **ω** is beyond 1.7. At the lower end of the molar ratio when the water availability is limited, the size of primary particles appears to monotonically approach a number of 3.6 ± 0.4 nm. At the other end of the molar ratio spectrum, it is understandable that as more water molecules become available for aerosol dynamics through coalescence and coagulation processes, the primary particles would become larger.

3.4. Model primary particles

Koch and Friedlander [27] described the coalescence process as a volume diffusion driven reduction in surface area.

$$\frac{da}{dt} = -\frac{\left(a - a_{sph}\right)}{\tau_f} \tag{2}$$

The surface area of the coalescing particle, a, is initially that of two equal spherical particles, a_0. The surface area is driven to that of a perfect sphere, a_{sph}, of equivalent volume, over time. The characteristic fusion time, τ_f, is dictated by material properties. Lehtinen and Zachariah [28] noted that Koch and Friedlander's approach had been successfully implemented into many models but under-predicted the primary particle size in certain cases. In the failed cases, the predicted primary particle sizes were approximately a few nanometers while the true primary particle sizes were much larger.

Zachariah, et al. [29] observed elevated particle temperatures, T_p, during the coalescence process in molecular dynamics simulations. Since coalescence is driven by volume diffusion with an Arrhenius function of temperature, they proposed a correction to the characteristic fusion time to account for the particle temperature dependence. The new definition presented in Lehtinen and Zachariah [30] is appropriate for both solid and liquid-state particles.

$$\tau_f\left(T_p\right) = \frac{3k_B T_g N}{64\pi\sigma_p D\left(T_p\right)} \tag{3}$$

In (3), T_g is the ambient gas temperature, N is the number of atoms per coalescing particle, σ_p is particle surface tension or surface free energy, and D is the self-diffusion coefficient. The Arrhenius form of the diffusion coefficient is

$$D\left(T_p\right) = D_o \exp\left(-\frac{E_a}{RT_p}\right) \tag{4}$$

In (4), D_o is the pre-exponential diffusion constant and $\mathbf{E_a}$ is the activation energy for volume diffusion. The universal gas constant is represented by R. Particle temperature was calculated in Lehtinen and

Zachariah[30] by performing an energy balance on two coalescing particles.

$$\frac{dT_p}{dt} = \frac{\sigma}{2c_p N \tau_f}\left(a - a_{sph}\right) - \frac{P_g c_g a_{sph}}{2c_v N\sqrt{2\pi m_g k T_g}}\left(T_p - T_g\right) - \frac{\varepsilon \sigma_{SB} a_{sph}}{2c_p N}\left(T_p^4 - T_g^4\right) \quad (5)$$

The first term on the right-hand side of (5) accounts for the surface energy released as surface area is decreased. The second term accounts for heat loss as the particle collides with the ambient air molecules. Here, ambient pressure is denoted by P_g and m_g is the mass of a gas molecule. The heat capacity of the particle, at constant volume is denoted c_p and c_g is the heat capacity of the ambient gas. The last term accounts for radiative losses to the environment, where ε is the emissivity and σ_{SB} is the Stefan-Boltzmann constant (5.67×10^{-8} W m^2 K^{-4}). The radiative term was introduced by Lehtinen and Zachariah.[30] Equations (2) through (5) were combined to define a set of two, coupled, **o**rdinary **d**ifferential **e**quation**s** (ODEs) that can be solved for transient particle size and particle temperature. Using this approach, Lehtinen and Zachariah were able to model similar particle temperatures during the coalescence process as those observed in molecular dynamics simulations.

Lehtinen and Zachariah[30] improved upon previous works by introducing a simple growth relation from Kruis et al.[31] to calculate particle temperatures over a series of collisions instead of modeling only a single collision event. The times at which the nth binary collision occurs, t_{coll_n}, is given by

$$t_{coll_n} = \frac{\frac{6}{5} v_0^{\frac{5}{6}}\left(n^{\frac{5}{6}} - 1\right)}{2.228\phi}\sqrt{\frac{\rho_p}{6kT}}\,. \quad (6)$$

The initial particle volume is denoted as v_0, ρ_p is the particle density, k is the Boltzmann constant (1.38×10^{-23} J K^{-1}), and ϕ is the particle volume loading (volume of particles divided by volume of gas). All particles are assumed to undergo simultaneous binary collisions; at every collision time, the entire aerosol concentration is halved, particle volume doubles, and particle surface area doubles. The first collision event occurs at time zero. Each subsequent collision is denoted by n.

Particle volume is calculated from the particle molecular weight, MW_p, Avogadro's number, N_{avg}, particle density, and the number of molecules in a coalescing particle.

$$v_{sph} = \frac{N \cdot MW_p}{N_{avg} \cdot \rho_p}\,. \quad (7)$$

Particle diameter is then calculated assuming the coalesced volume is spherical: $v_p = (\pi/6)d_p^{\,3}$.

For the first time step, the initial temperature of the particle, $T_{p,0}$, was calculated to be that prior to the collision plus the contribution from the energy released due to surface area reduction.

$$T_{p,0} = T_g + \frac{\sigma\left(a_0 - a_{sph}\right)}{2Nc_v} \quad (8)$$

The initial particle surface area was taken as twice the surface area of a monomer, N=1 in Eq. (7). The coupled ODE's were then solved in MATLAB® between $t_{coll,1}$ and $t_{coll,2}$. Equation (2) shows that the change in surface area is driven by the difference between the actual surface area and the surface area of an equivalent sphere. If the time between collisions is long relative to the characteristic fusion time, the surface area will asymptotically approach a_0. Thus, the normalized excess surface area is used as a convergence criterion to determine if the coagulation event resulted in coalescence.

$$a^* = \frac{a - a_{sph}}{a_0 - a_{sph}} \quad (9)$$

If $a^* < 0.05$, the collision was said to have resulted in complete coalescence.

A graphical example of this will be provided below. First, we provide the material property data used in simulations for UO_2F_2. Where possible, literature values for UO_2F_2 were used. Where no specific UO_2F_2 material property data were available, data for UO_2 were used. Material property data, and literature references, are provided in Table 2.

Table 2. Gas and particle properties used to simulate the evolution of particle size and particle temperature of coagulating and coalescing UO_2F_2 particles. References are given for uranium species. * The value of 4.86×10^{-4} was determined by this study as described below.

Model Parameter	Symbol	Assumed Value	Units
Gas pressure	P_g	101325	Pa
Gas temperature	T_g	293.15	K
Gas heat capacity	c_g	4.14×10^{-23}	J K^{-1}
Particle emissivity	ε	1	-
Gas molecular mass	m_g	4.81×10^{-23}	kg
Particle surface tension	σ_p	1.4 [32]	J m^{-2}
Particle density	ρ_p	6370 [33]	kg m^{-3}
Particle self-diffusion pre-exponential coefficient	D_0	4.3×10^{-8} [34]	m^2 s
Particle self-diffusion activation energy	E_a	4.86×10^4 [*]	J mol^{-1}
Particle heat capacity	c_p	4.14E-23 [28]	J K^{-1}
Particle molecular weight	MW_p	0.30802	kg mol^{-1}

The simulated particle diameter, d_p, is shown as a function of time in Figure 7. These simulated data were generated from solutions of equations 2 through 8. At approximately 4×10^{-6} seconds, two monomers were assumed to coalesce. The coupled ODEs were then solved for particle size and temperature until the time of the second collision. Each time step was solved separately, in succession, and particle size at the end of the time step was used to determine if particle coalescence had ceased or would continue. A circular symbol is shown in Figure 7 to show the final particle size.

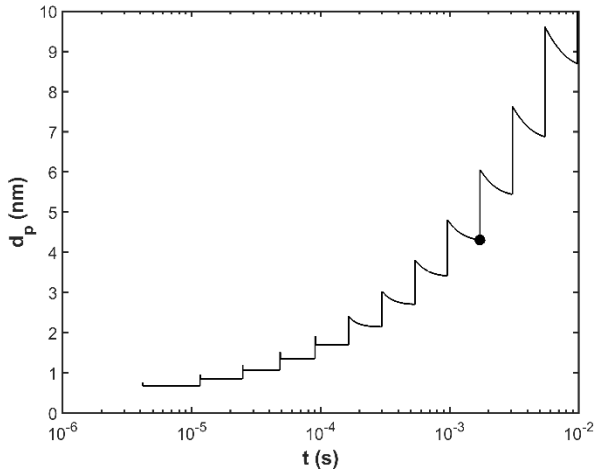

Figure 7. Simulated particle diameter (d_p) as a function of time (t) for coagulation and coalescence at 293.15K, 1 atm, and 2×10^{-7} m^3/m^3 volume loading. Discontontinuities occur at each collision time under the binary collision approximation; at t_{coll}, the surface area doubles instantaneously as two particles of equal surface area collide. These jumps are seen as vertical lines in the graph. The cessation of particle coalescence is marked with a circular symbol. This is the point at which the normalized excess surface area is less than 95%.

Figure 8 is provided to help illustrate the process being simulated. The surface area at the end of the last time step is denoted a_{old}. At the time of collision, two particles collide, and the surface area jumps to 2 x a_{old} = a_0. This is seen as a vertical jump in the data at the collision time: 9.6 x 10^{-4} seconds. The area a_0 is the initial condition for the ODE solve for surface area as a function of time a(t). The surface area at the end of the time step is denoted a_{new}. The surface area for a completely coalesced particle can be shown to be $a_{sph} = a_0 / (2^{1/3})$. The perfectly coalesced particle surface area, a_{sph}, is also shown. The particle is assumed to be coalesced if the difference between a_{new} and a_{sph} is small relative to the difference between a_0 and a_{sph}. Here, $a^* < 0.05$ was taken as coalesced.

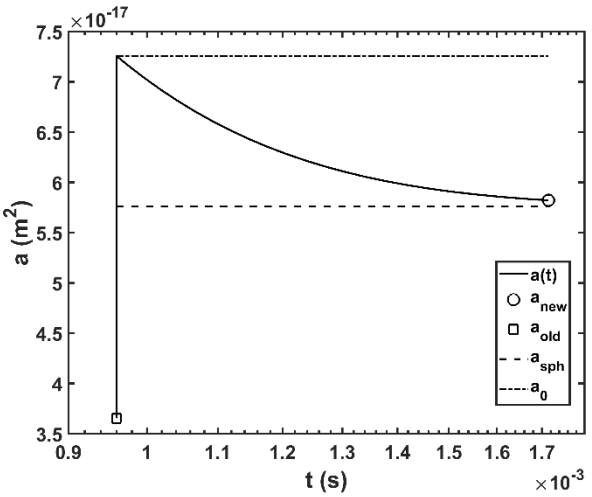

Figure 8. Process description of particle surface area in time: at the end of the previous time step the area is denoted a_{old}. A discontinuous jump in particle surface area occurs at approximately 0.96 x 10^{-3} seconds when two particles of size ~3.6 x 10^{-17} m^2 collide and form a new particle with double the surface area.

Simulated particle temperatures are shown in Figure 9. The temperature spikes are the result of energy added to the particle bulk from the reduction in surface area and associated energy. The temperature quickly drops due to radiative losses and energy losses due to collisions with gas molecules. The effect of rising temperature enhances coalescence as the self-diffusion coefficient increases with temperature. An expanded view of the second temperature spike is shown in the upper right-hand corner of the figure.

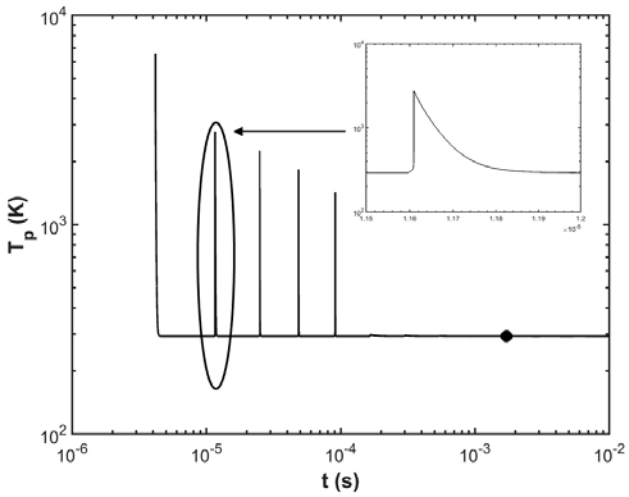

Figure 9. Simulated particle temperature (T_p) vs. time (t) for coagulation and coalescence at 293.15K, 1 atm, and 2x10^{-7} m^3/m^3 volume loading. The temperature spike near 10^{-5} seconds is expanded in the upper right-hand corner of the figure. The cessation of particle coalescence is marked with a circular symbol. This is the point at which the normalized excess surface area is less than 95%.

The primary technical challenge to this modelling effort is the lack of data, and uncertainty in available data, for parameters like D_0, E_a, and σ. Initially, E_a was taken from Auskern and Belle[34] as 8.8x10^{-4} J mol^{-1}. Due to the low volume loading, 2x10^{-7} m^3/m^3, low gas temperature, and high activation energy, no coalescence was observed. At ambient temperature, higher volume loading (on the order of 10^{-3}) would result in coalescence. Since our volume loading and gas temperature were well-known, E_a was allowed to vary in order to see if reasonable values would result in primary particle size predictions which agreed with experiments. A plot of primary particle size vs. Ea/R is shown in Figure 10. For large Ea/R, primary particles consist mostly of monomers and dimers. No coalescence is observed since self-diffusion must overcome a high energy barrier. At low Ea/R, all particles begin to coalesce similar to liquids. This analysis shows that 5800 < Ea/R < 5900 gives good agreement with experimental data ($d_{primary}$ = 3.6 nm).

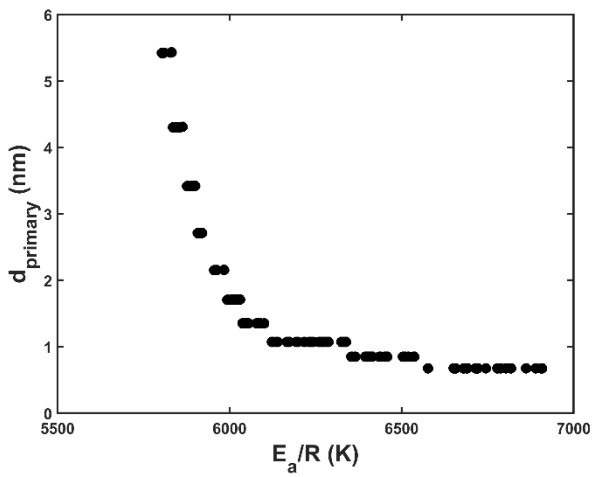

Figure 10. Primary particle size ($d_{primary}$) plotted agaist the ratio of the self-diffusion activation energy to the ideal gas constant (E_a/R). A value of 5800 < Ea/R < 5900 K results in a simulated primary particle size of approximately 3.4 to 4.3 nm.

The self-diffusion coefficient was calculated at a temperature of 1273K to determine if 5850 J mol^{-1} (derived from Figure 9) resulted in reasonable values. The choice of 1273 K was somewhat arbitrary but consistent with other works[34,35]. Results are shown in Figure 11. A self-diffusion coefficient of approximately 4x10^{-10} m^2/s gives a predicted primary particle diameter in the 3-4 nm range. The self-diffusion constant for SiO_2 is on the order of 1x10^{-9}

m^2/s [29] and $1x10^{-9}$ m^2/s for NaCl [35]. The values derived from Auskern and Belle give a self-diffusion constant much lower for uranyl ion diffusion in UO_2 ($1x10^{-21}$ m^2/s). Values for the anion and cation often vary considerably where the lattice structure is one parameter affecting diffusivity values. Based upon data for NaCl and SiO_2, the value derived here for UO_2F_2 aerosol particles seems reasonable. This also leaves room for model improvement; i.e., experimental determination of the self-diffusion value of the UO_2F_2 aerosol particles as temperature and particle composition varies.

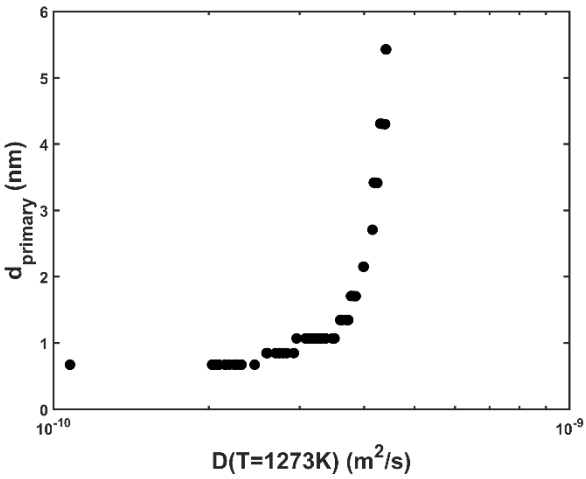

Figure 11. Primary particle size ($d_{primary}$) plotted agaist the self-diffusion coefficient (D; taken at 1273K). A self-diffusion coefficient on the order of $D=4x10^{-10}$ m^2/s results in a primary particle size ranging from 3.4 to 4.3 nm.

This model is based upon the simplifying assumption of binary collisions: at any given point in time there exists only one particle size and all particles of that size collide with a counterpart at the exact same time. We recognize that systems of interest are polydisperse, that is, there exists a distribution of particle sizes which collide at different rates and times dependent upon their sizes. We also acknowledge that multi-body coalescence may occur for non-coalesced particles that contain more than two sub-particles. Any model which includes the aforementioned effects would likely be less granular than the current model. More work is needed to determine how a model which includes polydispersity and multi-body effects would differ from the model presented herein.

4. Conclusions

We conclude that the formation and growth of aerosol particles by gas-phase UF_6 hydrolysis is strongly dependent on the availability of water molecules in our reactor conditions. The total number concentration of the UO_2F_2 particulate material that could be produced in the hydrolysis reaction is also regulated primarily by the availability of water molecule concentration. The higher the water molecule concentration, the higher number and larger of UO_2F_2 aerosol particles that could be produced. The growth rates of aerosol particles appear to approach a single number in the range of [0.05 ± 0.03 - 0.08 ± 0.04] (nm/s), statistically, as the molar ratio becomes smaller than 1. The size of primary particles from the UF_6 hydrolysis at water-deprived condition was estimated to be 3.6 ± 0.4 nm, the higher the availability of water molecules the larger the primary particles. Using a reasonable value for the activation energy of self-diffusion, the primary particle model developed in this work predicted a size range for the UO_2F_2 primary particles similar to that estimated from experiments. This result strongly suggests that the volume-driven coalescence process assumption used in the derivation of the primary particle model was reasonable. It is noted that there are questions remaining as to the chemical pathways and energetics of the nucleation process leading to the formation of the primary particles. The ability to precisely control the availability of water molecules in the reaction could lead to the production of nearly monodispersed aerosol particles. In other words, the result suggests that one can precisely manipulate the size of UO_2F_2 aerosol particles by controlling the water vapor availability and interaction of water molecules with UF_6 in the reaction. This finding has significant implications in the engineering manufacturing of fuel powder materials and possibly to future development and deployment of environmental sampling apparatus.

Conflicts of interest

The authors declare no conflicts of interest.

Acknowledgements

The authors acknowledge the technical assistance of Hal Jennings, Chris Boring, and Rocky Estes Jr., and appreciate valuable discussions with Paula Cable-Dunlap, Jennifer Ladd-Lively, Andrew Miskowiec, and Roger Kapsimalis. The authors appreciate comments and technical discussions of the anonymous reviewers. This research was supported by the National Nuclear Security Administration of the Department of Energy. Oak Ridge National Laboratory is managed by UT-BATTELLE, LLC for the U.S. DEPARTMENT OF ENERGY under contract DE-AC05-00OR22725. Sandia National Laboratories is a multi-mission laboratory managed and operated by National Technology & Engineering Solutions of Sandia, LLC, a wholly owned subsidiary of Honeywell International Inc., for the U.S. Department of Energy's National Nuclear Security Administration under contract DE-NA0003525.

References

[1] R. Hou, T. Mahmud, N. Prodromidis, K.J. Roberts, R.A. Williams, D.T. Goddard and T. Semeraz, *Ind. Eng. Chem. Res*., 2007, **46**, 2020-033.

[2] M. C. Lind, S. Garrison, and J. C. Becnel, *J Phys Chem A*, 2010, **114**, 4641-4646

[3] R. S. Kemp, *Sci Global Security*, 2008, **16**, 115-125.

[4] R. S. Kemp, *Ann Rev. Earth Planet. Sci.*, 2016, **44**, 17-35

[5] R. W. Kessie, *I&EC Process Design Develop*., 1967, **6**, 105-111.

[6] W. D. Bostick, W. H. McCulla, P. W. Pickrell, D. A. Branam, S*ampling and characterization of aerosols formed in the atmospheric hydrolysis of UF6*, Report K/PS-5027; Oak Ridge Gaseous Diffusion Plant, 1983.

[7] W. D. Bostick, W. H. McCulla, and P. W. Pickrell, *Sampling, characterization, and remote sensing of aerosols formed in the atmospheric hydrolysis of uranium hexafluoride*, Report K/PS-5042; Oak Ridge Gaseous Diffusion Plant, 1984.

[8] R. Kips, A. Leenaers, G. Tamborini, M. Betti, S. Van den Berghe, R. Wellum, and P. Taylor, *Microsc. Microanal*. 2007, **13**, 156-164.

[9] R. S. Kips and M. J. Kristo, *J. Radioanal. Nucl. Chem*. 2009, **282**, 1031-1035.

[10] P. W. Pickrell, *Characterization of the solid, airborne materials created by the interaction of UF6 with atmospheric moisture in a contained Volume*, Report K/PS-144; Oak Ridge Gaseous Diffusion Plant, 1982.

[11] P. W. Pickrell, *Characterization of the solid, airborne materials created by the interaction of UF6 with atmospheric moisture in a contained Volume*, Report K/PS-915; Oak Ridge Gaseous Diffusion Plant, 1984.

[12] P. W. Pickrell, *Characterization of the solid, airborne materials created when UF6 reacts with moist air flowing in single-pass mode*, Report K/PS-1134; Oak Ridge Gaseous Diffusion Plant, 1985.

[13] W. Schotte, *Ind. Eng. Chem. Res*., 1987, **26**, 300-306.

[14] S. R. Hanna, D. G. Strimaitis and J. C. Chang, *J. Hazardous Mater*., 1991, **26**, 127-158.

[15] H. W. M. Witlox, *Atmos. Environ*., 1994, **28**, 2917-2932.

[16] H. W. M. Witlox, *Atmos. Environ*., 1994, **28**, 2933-2946.

[17] M. H. West and K. M. Axler, *Thermodynamic Modeling of Hydrogen Fluoride Production Relevant to Actinide Residue Treatment*, Las Alamos National Lab Report, LA-12909-MS, 1995.

[18] S. G. Giannissi, A. G. Venetsanos, N. Markatos, and J. G. Bartzis, *J Loss Prevention in the Process Industries*, 2013, **26**, 245-254.

[19] S.-W. Hu, X.-Y. Wang, T.-W. Chu, and X.-Q. Liu, *J. Phys. Chem*., 2008, **112**, 8877-8883.

[20] S.-W. Hu, X.-Y. Wang, T.-W. Chu, and X.-Q. Liu, *J. Phys. Chem.*, 2009, **113**, 9243-9248.

[21] S.-W. Hu, H. Lin, X.-Y. Wang, and T.-W. Chu, *J. Molecular Struct.*, 2014, **1062**, 29-34.

[22] F. R. Quant, R. C. Flagan, and K. D. Horton, *J Aerosol Sci.*, 1993, **24**, Suppl 1, S83-S84.

[23] D.-R. Chen, D. Y. H. Pui, G. W. Mulholland, and M. Fernandez, *J Aerosol Sci*., 1999, **30**, 983-999.

[24] J. C. Anderson, C. P. Kerr, and W. R. Williams, *Correlation of the Thermophysical Properties of UF6 over a Wide Range of Temperature and Pressure*, Oak Ridge National Laboratory Report, ORNL/ENG/TM-51, 1994

[25] Cheng, M.D., *J Atmos. Chem*., 2018, **75**, 1-16.

[26] G. L. Wagner, S. A. Kinkead, M. T. Paffett, K. D. Rector, B. L. Scott, A. L. Tamasi, and M. P. Wilkerson, *J. Fluorine Chem*., 2015, **178**, 107-114.

[27] W. Koch and S. K. Friedlander, *J Colloid Interf Sci*, 1990, **140**, 419-427.

[28] M. R. Zachariah, M. J. Carrier and E. BlaistenBarojas, *J Phys Chem*, 1996, **100**, 14856-14864.

[29] M. R. Zachariah and M. J. Carrier, *J Aerosol Sci*, 1999, **30**, 1139-1151.
[30] K. E. J. Lehtinen and M. R. Zachariah, *Phys Rev B*, 2001, **63**, 205402.
[31] F. E. Kruis, K. A. Kusters, S. E. Pratsinis and B. Scarlett, *Aerosol Sci. Technol*., 1993, **19**, 514-526.
[32] P. W. Tasker, Surf Sci, 1979, **87**, 315-324.
[33] N. Leclaire and S. Evo., *Definition of a new UO2F2 density law for low-moderated solution (H/U<20) and consequence on criticality safety, Institute for Radiological Protection and Nuclear Safety*, Saint-Petersbourg, France, 2007.
[34] A. B. Auskern and J. Belle, *J. Nuclear Materials,* 1961, **3**, 311-319.
[35] D. Mapother, H. N. Crooks and R. Maurer, *J Chem Phys*, 1950, **18**, 1231-1236